Li, Y. & Bolton, M. (2014). *Géotechnique* **64**, No. 6, 419–430 [http://dx.doi.org/10.1680/geot.13.P.197]

Energy conservation validates deformation mechanisms around model cantilever wall excavations in sand

Y. LI*† and M. BOLTON†

Based on soil movement measurements in two centrifuge models simulating cantilever wall excavation in dense and loose sand respectively, simplified deformation mechanisms are proposed on both sides of the wall. Negative dilation angles are used in the mechanism to model sand volume change at a moderate strain level corresponding with the typical serviceability limit of facilities on the retained ground within the zone of influence of the wall. An energy calculation is then performed for each of the two centrifuge tests to check the internal consistency of the inferred deformation mechanisms, and the adequacy of the stress–strain model used for the sand. It is found that energy balances within an error of 7% in both tests. The major energy flow happens on the active side of the wall, where the potential energy loss is roughly equal to the work done due to sand shear and contraction. The energy stored in wall bending and the energy lost due to boundary friction are small in comparison. The validated model of the settlement and shearing of the retained ground is then used to illustrate how to assess the degree of building damage in relation to angular distortion and tensile strain in the retained ground supporting its shallow foundations.

KEYWORDS: centrifuge modelling; deformation; excavation; retaining walls; sands; soil–structure interaction

INTRODUCTION

A key goal of physical modelling is to observe and validate simplified mechanisms for use in design. Insufficient attention has been paid in the past to the use of soil stress–strain data, and boundary movements, in demonstrating that such mechanisms are internally consistent and properly understood. The first aim of this paper is to assess the possible role of the principle of energy conservation in the validation of these mechanisms. As an example, the behaviour of a simple cantilever wall retaining dry sand, subject to in-flight excavation in a centrifuge, is chosen.

The ground movements adjacent to an excavation in sand have been presented by many researchers (e.g. Peck, 1969; Clough & O'Rourke, 1990). Following Peck (1969) the width of the zone of influence of an excavation has generally been normalised by the depth of excavation, although Osman & Bolton (2004) and Lam & Bolton (2011) have shown that, in clays, the deformation mechanism could better be scaled by the depth of soft clay within which an excavation is made. Although Bransby & Milligan (1975) provide information on the deformation mechanisms around an excavation in sand, they pertain to models tested at 1***g*** (and therefore to stresses which are an order of magnitude smaller than those relating to the field), and to large shear strains (resolvable only to 1% with the photographic measurements that were then available). Their mechanistic analysis was accordingly fitted to the data of sand dilating at its peak strength, rather than being appropriate to serviceability issues.

The potential damage to buildings adjacent to excavations was considered by Boscardin & Cording (1989). For example, a limiting angular distortion of 2×10^{-3} should generally avoid 'moderate to severe damage' in masonry walls. This would correspond approximately to the distortion created when a stiff, 20 m deep, retaining wall moves out 40 mm at its crest, creating a corresponding maximum settlement of 40 mm and a zone of influence about 20 m wide, within which are located the shallow foundations of a wide building. If the ground were shearing at constant volume, and moving on planes at 45° to the vertical, this would also correspond with a soil shear strain of 0·4%. The second aim of the paper is to portray excavation mechanisms for sand under full-scale stresses in a centrifuge model, focusing on serviceable shear strains in the range 0–0·4%. The approximate relationships between wall movement and building damage, referred to above, can then be refined.

PHYSICAL MODELLING OF CANTILEVER WALL EXCAVATIONS

Two centrifuge models were tested at 60***g*** to simulate cantilever wall excavations in sand; deformations were intended to be in plane strain. Dry Hostun sand was prepared in a rectangular test box with the Cambridge sand pourer (Madabhushi *et al.*, 2006): loose sand at relative density $I_D \sim 0{\cdot}45$ and dense sand at $I_D \sim 0{\cdot}85$. According to Stringer (2012), the Hostun sand has a minimum void ratio of 0·555 and a maximum void ratio of 1·067. It has a specific solid density of 2·65 and a critical state angle of 33°. The average of five single-particle optical sizing (SPOS) distribution tests gave size characteristics $D_{10} = 0{\cdot}300$ mm, $D_{60} = 0{\cdot}491$ mm so the uniformity coefficient (D_{60}/D_{10}) was 1·637.

A schematic view of the test set-up is shown in Fig. 1. A two-axis servo-actuator (Haigh *et al.*, 2010) was installed on top of the test box to control in-flight excavation. A T-shaped scraper was attached to the sliding housing of the actuator to perform in-flight sand scraping. The retaining wall was

Manuscript received 19 November 2013; revised manuscript accepted 11 April 2014. Published online ahead of print 5 June 2014.
Discussion on this paper closes on 1 November 2014, for further details see p. ii.
* Schlumberger China S.A., ChaoYang District, Beijing, People's Republic of China. Tragically, Dr Yuchen Li went missing on Malaysia Airlines flight MH370 on Saturday, 8 March 2014, just three weeks after this paper was given qualified approval for publication. Dr Li was returning to the Beijing office of Schlumberger after attending an initial training course in Kuala Lumpur.
† Geotechnical and Environmental Group, University of Cambridge, Schofield Centre, Cambridge, UK.

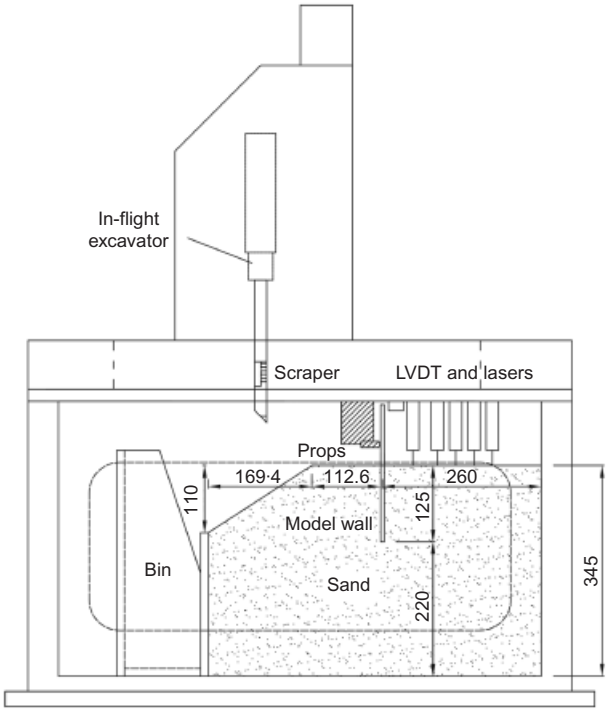

Fig. 1. Schematic view of a typical 1/60 scale model (dimensions in mm)

modelled by a 6 mm thick milled aluminium plate. It had an equivalent bending stiffness at prototype scale of $2{\cdot}68 \times 10^8$ N m^2/m using a scale factor of 60^3 following Powrie (1986), corresponding to a heavy-duty sheet pile wall. During both tests, the initial embedment depth was 160 mm corresponding to 9·6 m at full scale. Strain gauges were glued on the centreline of the wall to measure bending moments. A waste bin was provided that could be fed by scraping sand onto a slope that was sufficiently far away from the wall not to significantly modify initial conditions. During the tests, the excavator scraped sand layer by layer from in front of the wall until the designed excavation depth was reached.

Two digital cameras (Canon Powershot G10, 14·7 megapixels) were installed to take pictures on either side of the wall through a Perspex window. Particle image velocimetry (PIV) was used to calculate the soil movements beside the wall during the excavation. The details of the method were introduced by White *et al.* (2003).

Soil movements during excavation were measured by PIV after every layer of scraping. Overall soil displacements after the whole excavation are shown in Fig. 2. Note the difference in displacement scale between the vector plots. Soil movements observed in the loose sand test were roughly ten times those in dense sand at similar excavation depths. In both plots, soil movements on the active side were much larger than on the passive side. In the loose sand test, soil mainly moved horizontally on the passive side. In the dense sand test, some vertical movements can also be observed close to the wall on the passive side, which are presumed to be caused by scraper penetration and scraping forces. Maximum ground movements in the loose sand test were about 5 mm, with the crest of the wall moving about 3% of the retained height. In the dense sand test, the maximum ground movements were about 0·4 mm, and the wall deflected about 0·2% of the total height, so measurement errors led to greater scatter.

Soil shear strain and volumetric strain can be derived by differentiation of neighbouring measured ground movements.

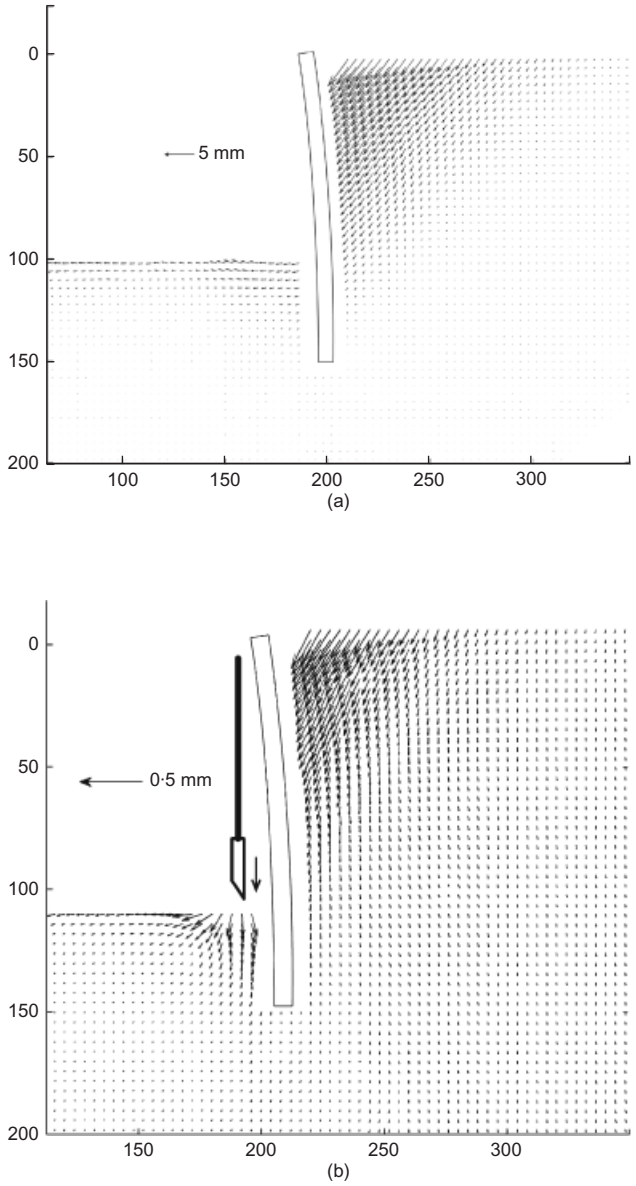

Fig. 2. Total ground movement in cantilever wall excavations: (a) loose sand excavated to 116 mm; (b) dense sand excavated to 117 mm (scales in mm)

Small random errors in displacement measurement can therefore lead to significant 'noise' in the plotting strains. Shear strains are analysed at different stages of the test on loose sand, as shown in Fig. 3. The cut-away corners in the figure are because of photographic distortions and reflections. Rectangles have been included to show the relative positions of the model wall. Significant soil shear strains are seen to be confined within a triangle defined by the retaining wall, the sand surface and an internal boundary line that extends to the wall toe.

Accumulated shear strains in the dense sand test are shown in Fig. 4. The shear strain field is not as clear as in Fig. 3 owing to the smaller soil movements in relation to a constant random error in measurement. However, Fig. 4(d) also shows that shear strain occurs predominantly within a triangle, with its hypotenuse extending approximately to the wall toe.

SIMPLIFIED SOIL DEFORMATION MECHANISMS

Analysis on experimental data

The significant soil movements in Fig. 2 are on the active side, and movement directions appear to be approximately

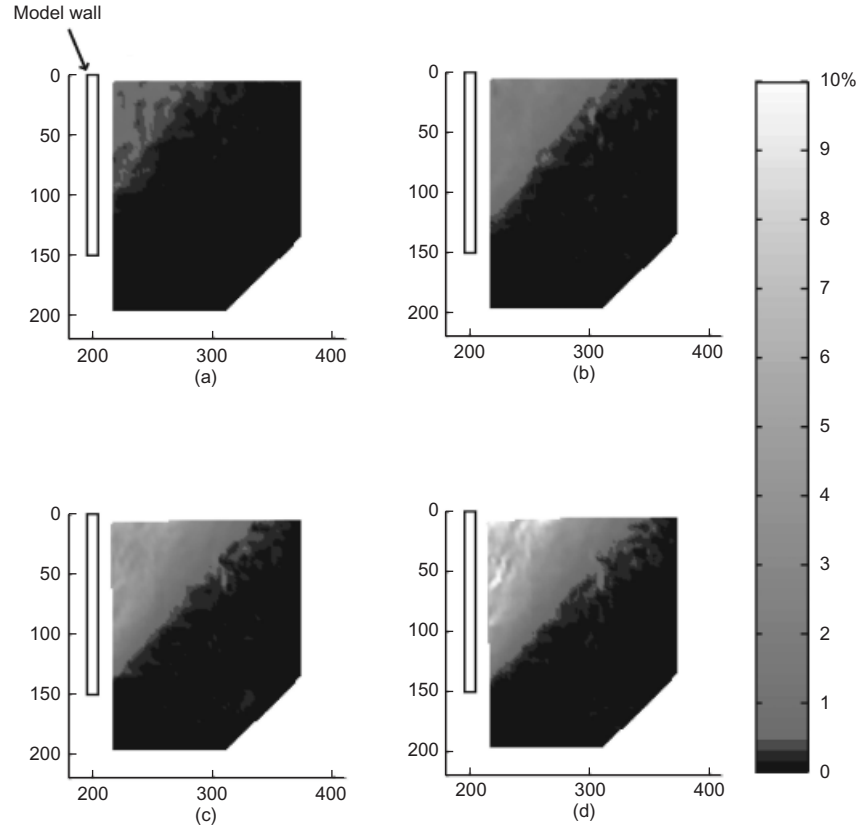

Fig. 3. Cumulative shear strains in loose sand, plotted after each of the four stages of excavation: (a) 0–80 mm; (b) 0–100 mm; (c) 0–112 mm; (d) 0–116 mm

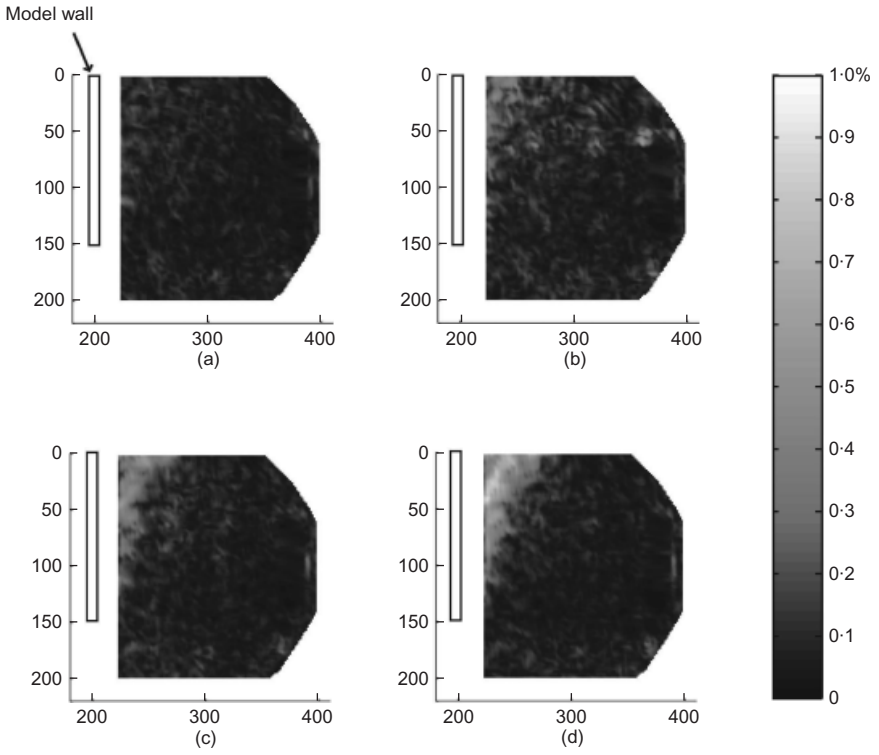

Fig. 4. Cumulative shear strains in dense sand, plotted after each of the four stages of excavation: (a) 0–81 mm; (b) 0–102 mm; (c) 0–111 mm; (d) 0–117 mm

parallel. Fig. 5 shows typical plots of vertical movement (v) against horizontal movement (u) for all PIV patches inside the active triangle in both tests. In each of the plots, all the displacement data scatter around a straight line through the origin, which confirms the impression in Fig. 2 that soil movements on the retained side are parallel. The scatter in Fig. 5 is $\pm 0{\cdot}06$ mm for vertical displacements up to a maximum of $1{\cdot}2$ mm in the loose sand (i.e. within $\pm 5\%$),

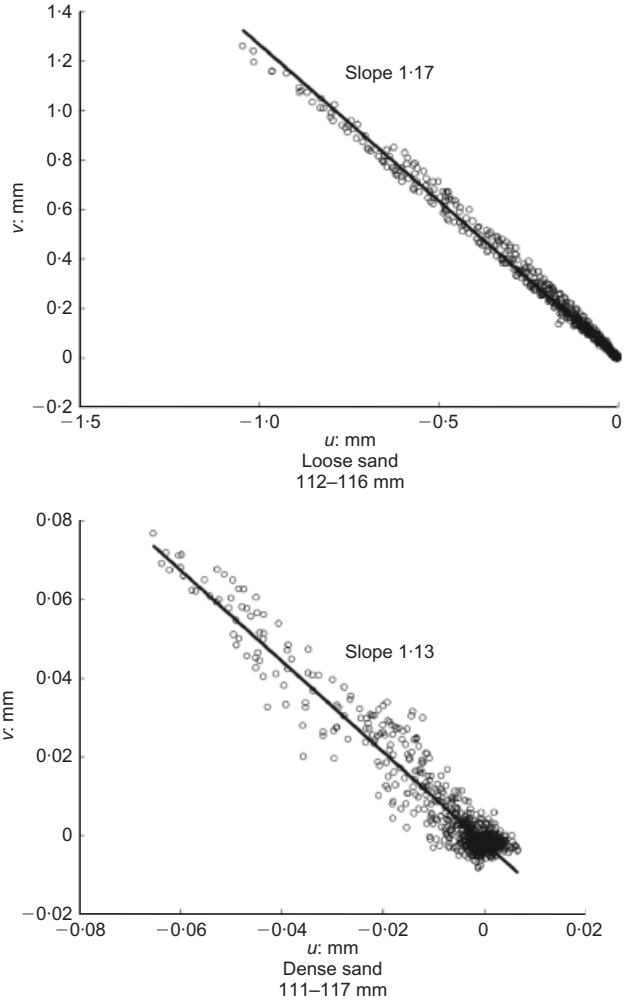

Fig. 5. Vector inclination at a typical stage in cantilever wall excavations

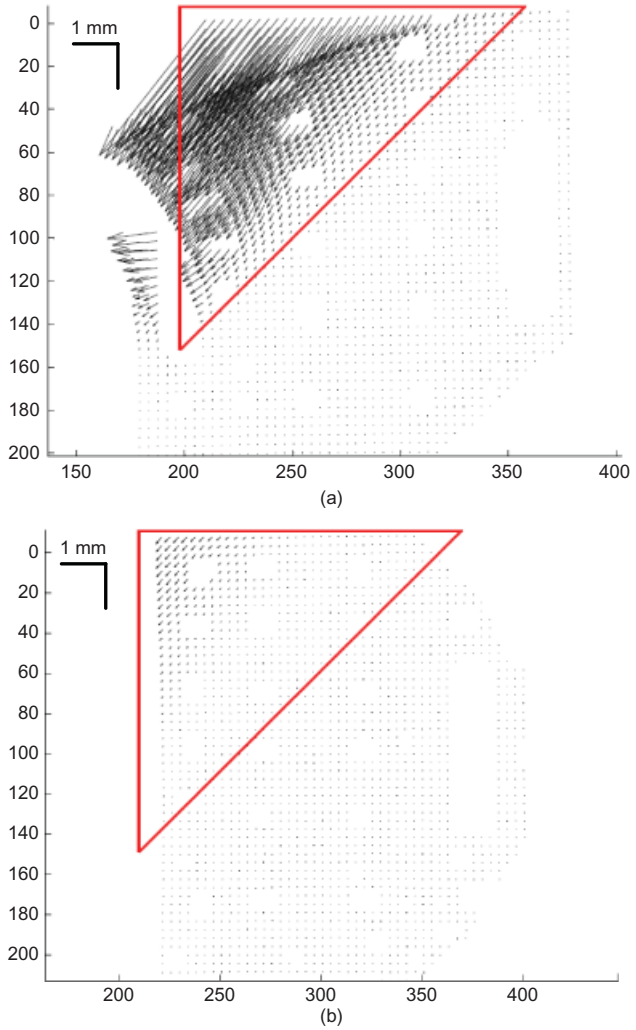

Fig. 6. Deformation range in cantilever wall tests: (a) loose sand (100–116 mm); (b) dense sand (111–117 mm) (scales in mm)

and ±0·025 mm for vertical displacements up to a maximum of 0·075 mm in the dense sand (i.e. within ±33%). Although the absolute uncertainty in the displacement correlation for dense sand is smaller than for loose sand, the actual magnitude of the displacements being measured in the dense sand is an order of magnitude smaller. This means that there is greater uncertainty in fixing the ratio v/u for the dense sand at 1·13 than that involved in establishing a gradient of 1·17 for the loose sand.

The value of the ratio v/u indicates the displacement directions of soil patches. Although the movement directions are parallel on the active side, the movement directions change at different stages in both tests. Initially a simplified mechanism will be used, to prepare for further analysis. An isosceles right angle triangle is drawn, formed by the wall, soil surface and a hypotenuse on the retained side. All the soil movements are initially assumed to occur inside the triangle. This triangle is similar to the deformation zone assumed in excavations in undrained clay (Osman & Bolton, 2004). Fig. 6 shows soil movement plots for typical stages of the excavation in the centrifuge tests, with an isosceles right triangle superimposed. Soil movements outside the triangle on the retained side are relatively small.

It is therefore reasonable to simplify the deformation as triangular zone OAB distorting to OAB′ as the wall rotates through angle β and the nearby soil surface rotates by α: see Fig. 7.

The horizontal strain in the triangle is given by

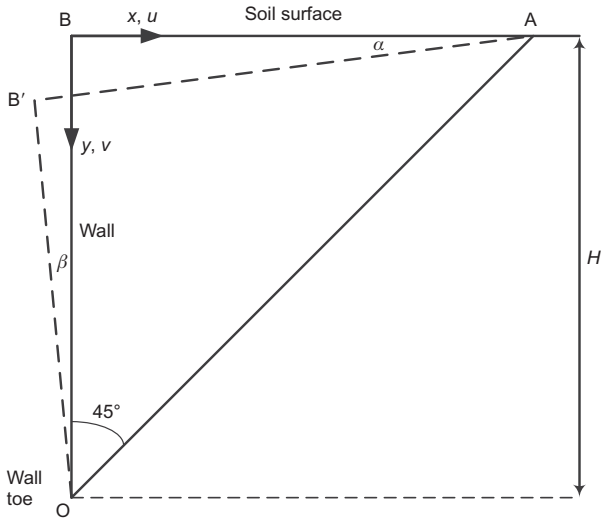

Fig. 7. Simplified triangular mechanism on the retained side

$$\delta\varepsilon_3 = -\frac{\beta H}{H} = -\beta \tag{1}$$

A column of movement vectors beside the wall is selected, and horizontal components (u) of these vectors are plotted against soil vertical position (y axis) so that β appears as the gradient.

The vertical strain in the triangle is given by

$$\delta\varepsilon_1 = \frac{\alpha H}{H} = \alpha \tag{2}$$

Similarly, a row of soil vectors at the soil surface is selected, and α is calculated from the gradient of the vertical components (v) plotted against horizontal position (on the x axis).

The average engineering shear strain increment can then be expressed as

$$\gamma = \delta\varepsilon_1 - \delta\varepsilon_3 = \alpha + \beta \tag{3}$$

At each stage, the average movement direction can be found by regression of the horizontal and vertical components of vectors in the triangle. The angle between the vertical and the average movement vector is plotted against average engineering strain and shown in Fig. 8(a). Unlike undrained clay, the sand movement direction is less than 45° from the vertical, implying a reduction in volume. At a small excavation depth in loose sand, the angle between the movement vector and the vertical is small, which implies significant contraction during shearing. When the excavation depth gets larger, the angle gets larger. In dense sand, the angles at each stage are closer to 45°, but the magnitude of shear strain remains small.

Rather than investigating further the relationship between soil displacement directions and shear strain, it is more profitable to derive a simplified mechanism for soil movements, with the average directions related to sand relative densities. This angle is chosen from Fig. 8(a) to be 29° in loose sand and 43° in dense sand. These angles pertain to an engineering shear strain of 0·4%, which is equivalent to 40 mm of lateral displacement and 40 mm of maximum settlement beside a stiff cantilever wall with a total depth of 20 m, according to the relationship derived by Bransby & Milligan (1975)

$$\delta\gamma = 2\theta\sec\nu \tag{4}$$

where $\delta\gamma$ represents the incremental shear strain, θ is wall rotation angle, and dilation angle ν is taken to be zero here for illustration purposes. This offers a feasible serviceability limit for structures resting on the retained soil, or utilities buried within it.

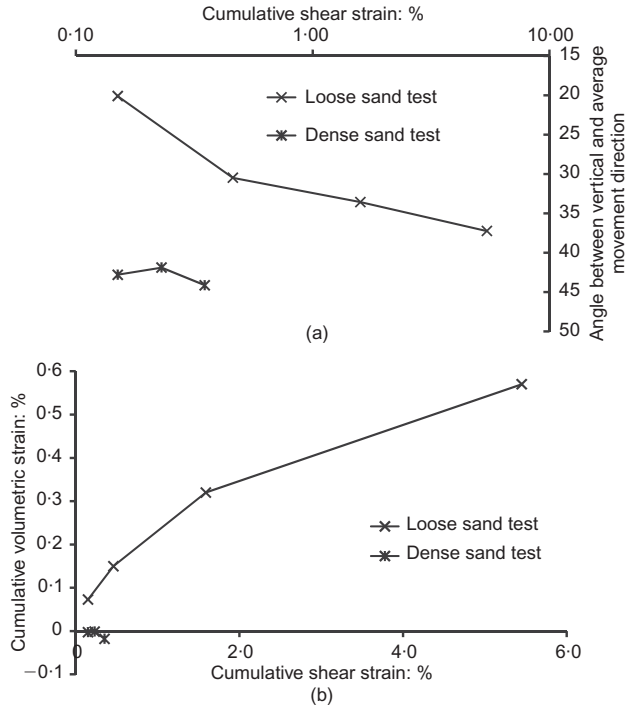

Fig. 8. Results of strain analysis using a simple 45° triangle: (a) soil movement directions; (b) volumetric strains

The total volumetric change within triangle OBA can be examined by checking the change in the area of the triangle stage by stage. As there is no measurable soil movement at the hypotenuse, the total volume decrease is equal to the area decrease due to settlement at AB, minus the area increase due to horizontal movement at OB. Fig. 8(b) shows the relationship between the cumulative volumetric strain and the cumulative shear strain, averaged over triangle OBA as excavation proceeds. During an excavation in loose sand, volumetric strains are positive throughout the test. The ratio between volumetric strain and shear strain is larger at small excavation depths. This means that there is a negative dilation angle which reduces in magnitude as strains increase. During an excavation in dense sand, volumetric strains are close to zero.

According to the previous analysis, a simple triangular deformation mechanism is assumed to accommodate soil shear strain and volume loss with fixed movement directions. Friction between the wall and the sand is ignored, so the direction of major principal stress is vertical on the retained side. The direction of the major principal strain increment is assumed to be vertical, to coincide with the direction of principal stress. If a constant dilation angle ($\nu = -\eta$) is assumed, the Mohr circles for stress before (solid line) and after (dashed line) a stage of excavation can be drawn as in Fig. 9(a), with the corresponding strains in Fig. 9(b). Here η is defined for convenience as the contraction angle, which is the negative angle of dilation. If η is chosen to be a fixed number everywhere on the retained side, zero extension lines are straight and at $45° + \eta/2$ clockwise from the vertical, according to the Mohr strain circle drawn in Fig. 9(b). The zero extension line OA through the wall toe will now be chosen as the new boundary between the deformed area and the unaffected area, so that no strain discontinuity occurs across this boundary. The movement vector of soil at B behind the wall crest is shown in Fig. 9(c), making angle η in relation to zero-extension direction P, and therefore an angle of $45° - \eta/2$ from the vertical. Consistent displacement vectors for representative points along the bisector BM of the deformation mechanism then reduce progressively to zero at point M.

According to the values picked from the experimental observations in Fig. 8(a), the contraction angles can be taken as $\eta = 32°$ in loose sand and $\eta = 4°$ in dense sand. This means that both triangles assumed for dense and loose sand are bigger than the 45° triangle initially assumed in the simplified triangular mechanism of Fig. 7. All measurable soil movements on the active side of the wall are now included in the refined mechanism in Fig. 9(c), whereas some measurable vectors fell just below the 45° hypotenuse of the simpler mechanism shown earlier in Figs 6(a) and 7.

A new coordinate system for the refined deformation mechanism is now constructed in Fig. 10 for soil displacements on the retained side of the wall. The new origin is at the top right corner of the triangle at A, with the X axis on the hypotenuse, directed towards the wall toe. Soil displacements U are taken to offer an angle η to zero-extension lines as indicated in Fig. 9(c). Therefore, in the new coordinate system, the ratio between the movement component U_X parallel to the X axis and movement component U_Y parallel to the Y axis is a constant ($\cot\eta$). It is assumed that the magnitude of movement is constant within any given elementary layer of sand (thickness δY) parallel to the hypotenuse. Although U_X does show some variation for the same Y coordinate, this is considered to be of secondary importance. For a thin layer of sand parallel to a zero extension line, the

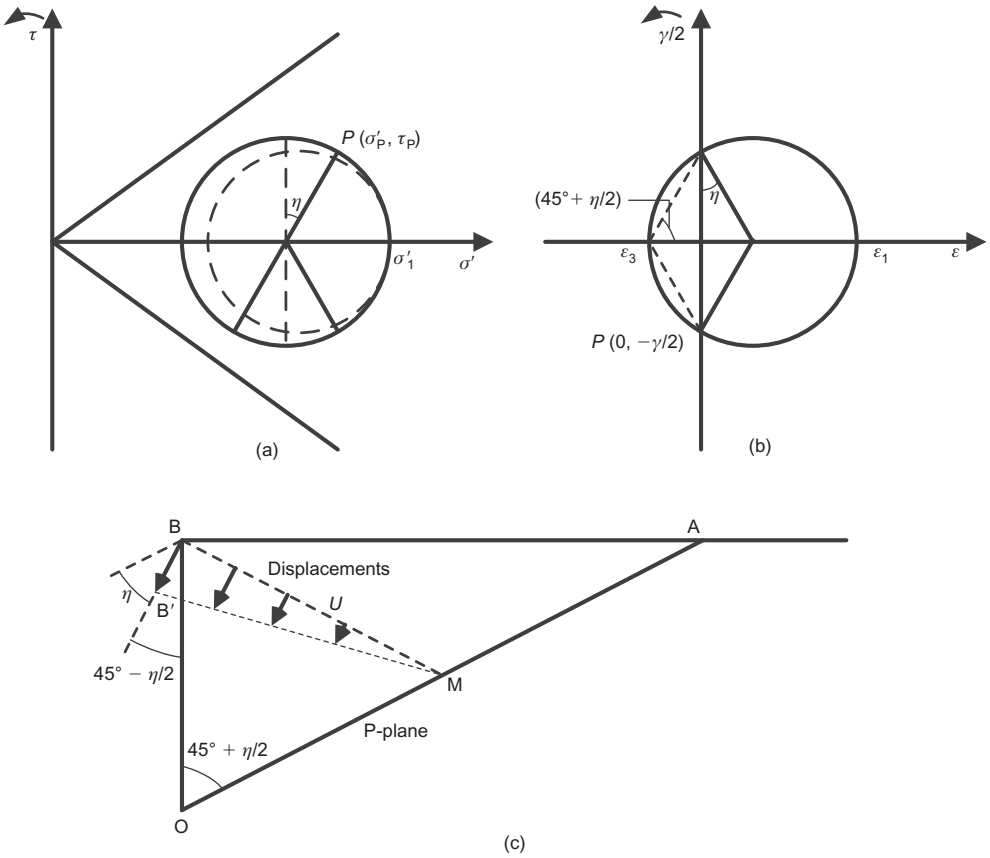

Fig. 9. Refined mechanism on the retained side of the wall: (a) stresses; (b) strains; (c) displacements

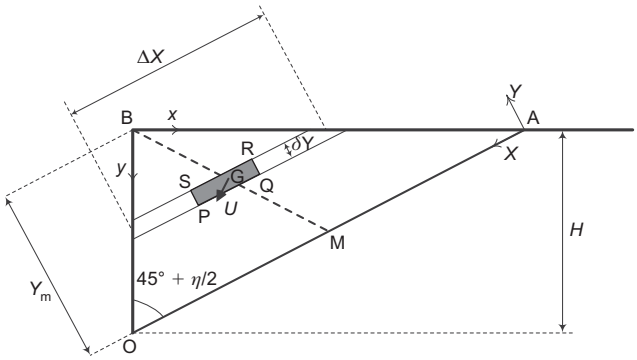

Fig. 10. Refined deformation mechanism: geometry for analysis

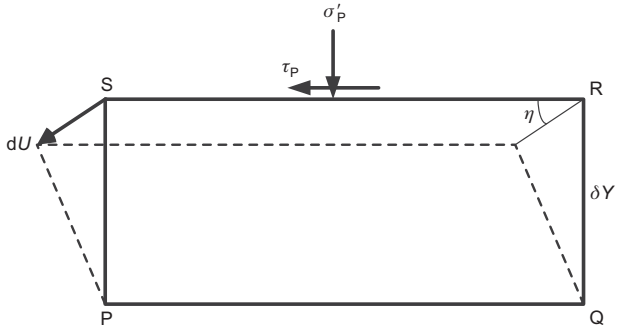

Fig. 11. A thin layer parallel to zero-extension P-lines in the mechanism

displacement U_X inside quadrilateral PQRS, which encloses the centroid G of each layer, is used to characterise the movement.

A central portion PQRS of the elementary layer (shaded in Fig. 10) is shown in Fig. 11. At each stage, the sand at the upper surface SR moves at angle η relative to sand at the lower surface PQ.

The shear strain increment is

$$\mathrm{d}\gamma = \frac{\delta U \cos\eta}{\delta Y} \tag{5}$$

The volumetric strain increment is

$$\mathrm{d}\varepsilon_{\mathrm{vol}} = \mathrm{d}\varepsilon_{\mathrm{P}} = \frac{\delta U \sin\eta}{\delta Y} \tag{6}$$

The previous assumption of wall rigidity can now be relaxed. A polynomial function of the second order (equation (7)) is found to be a simple and effective expression to fit the relationship between U_X and Y. The form of the fitting equation is selected so that U_X is zero at the mechanism boundary ($Y = 0$), and a maximum $U_{X\mathrm{m}}$ at the maximum Y coordinate value Y_{m}. $U_{X\mathrm{m}}$ and Y_{m} are used as normalisation factors so that function parameter c is dimensionless.

$$\frac{U_X}{U_{X\mathrm{m}}} = c\left(\frac{Y}{Y_{\mathrm{m}}}\right)^2 + (1-c)\frac{Y}{Y_{\mathrm{m}}} \tag{7}$$

The result of the fitting is shown in Table 1. It is seen that in each stage of each test, the fitting function parameter c lies in the range $1{\cdot}3 \pm 0{\cdot}15$. For simplicity, it is therefore assumed that the relationship between U_X and Y for sand at any density deforming in the small-to-moderate strain range behind a cantilever retaining wall similar to that used in the tests is

$$\frac{U_X}{U_{X\mathrm{m}}} = 1{\cdot}3\left(\frac{Y}{Y_{\mathrm{m}}}\right)^2 - 0{\cdot}3\frac{Y}{Y_{\mathrm{m}}} \tag{8}$$

Table 1. Fitting function parameters for $U_X - Y$ relationship

Excavation, h: mm	Loose sand test stages				Dense sand test stages		
	0–60	60–80	80–100	100–116	0–105	105–111	111–117
$U_{X\mathrm{m}}$: mm	0·13	0·32	1·21	4·07	0·165	0·08	0·14
c	1·15	1·30	1·36	1·41	1·24	1·31	1·41

When $Y/Y_\mathrm{m} < 0{\cdot}23$, soil movement U_X would be small, but it would be negative according to equation (8). However, in the experimental soil movement plots, negative movements (away from the wall) are not observed in the retained soil; instead, movements close to the wall toe in the region $Y/Y_\mathrm{m} < 0{\cdot}23$ are negligible. Therefore, the sand movement relationship is simply truncated in accordance with the data to obtain equation (9).

$$\frac{U_X}{U_{X\mathrm{m}}} = \begin{cases} 1{\cdot}3\left(\dfrac{Y}{Y_\mathrm{m}}\right)^2 - 0{\cdot}3\dfrac{Y}{Y_\mathrm{m}}, & \dfrac{Y}{Y_\mathrm{m}} > 0{\cdot}23 \\ 0, & \dfrac{Y}{Y_\mathrm{m}} \leqslant 0{\cdot}23 \end{cases} \tag{9}$$

With these assumptions, the simplified mechanism for soil movements on the retained side of the wall is now complete. This quadratic displacement function has been shown to provide an acceptable fit to the data of the model cantilever wall, representing a heavy-duty sheet-pile wall, embedded either in loose or dense sand. It accordingly allows a more accurate assessment to be made of the work done in deformation. It also provides a more realistic settlement profile on the retained soil surface, an aspect of crucial importance in estimating possible damage to nearby structures and services.

Deformation mechanism on the passive side of the wall

Little noticeable ground movement was observed on the excavated side of the wall, except for soil movements around the scraper, which are considered to be due to scraper penetration and dragging. However, a triangular mechanism is still assumed, as shown in Fig. 12. All soil movements on the excavated side are taken to be restricted within a 45° isosceles triangle and to be parallel, as shown in Fig. 12(a). The movement direction is taken to be 45° from the vertical. In each thin layer parallel to the hypotenuse, the soil movement is taken as constant. Fig. 12(b) shows the assumed deformation of the thin layer. Soil dilation is ignored on the excavated side, for simplification of the model and in view of the lack of information on the very small soil displacements. The horizontal movements of the wall at a given elevation are assumed to be the same as those of the sand on either side of the wall, so the magnitude of movement on the passive side can be estimated from the horizontal component of soil movement on the active side. These are very small, as indicated in Fig. 2, so further refinement was deemed unnecessary.

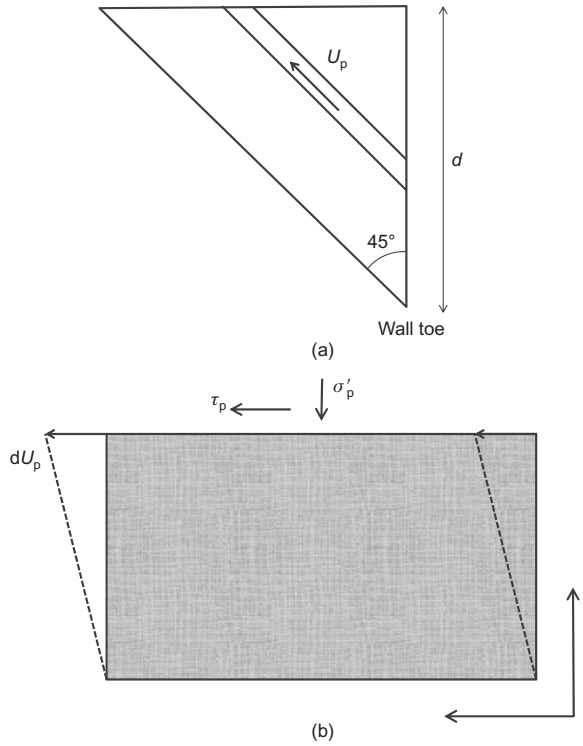

Fig. 12. Assumed movement mechanism on the passive side: (a) deformation mechanism on the passive side; (b) a thin layer parallel to the hypotenuse

ENERGY BALANCE FOR THE DEFORMATION MECHANISMS

The process of excavation can be regarded as transferring potential gravitational energy lost due to settlement, to work done deforming the soil and the wall. This energy flow in the two centrifuge tests will now be checked with respect to the simplified deformation mechanisms. Such an approach has proved valuable for excavation in clays (Lam & Bolton, 2011), but this is the first trial in sands.

At each stage, the gravitational energy loss should balance the work done on the sand and the elastic strain energy stored in wall flexure. In these tests, which were intended to deform in plane strain, the frictional energy dissipated at the contact surfaces between the sand and strongbox will also be estimated. However, as zero friction was assumed between the retaining wall and the sand in the mechanism analysed in Fig. 9, the influence of wall friction on the energy balance will also be ignored. Energy changes in the sand per unit length of wall can then be calculated slice by slice and summed.

Gravitational potential energy loss

The total gravitational loss of energy on the retained side of the wall, and the increase on the excavated side, are summed for each slice at each stage of the excavation. As the movements are the same for all sand particles in a given slice, the gravitational energy loss on the retained side ΔP_r can be expressed, referring to Fig. 10, as

$$\Delta P_\mathrm{r} = \sum_{\mathrm{layers}\_\delta Y}^{Y_\mathrm{m}} \gamma'_\mathrm{soil}\, \Delta X\, \delta Y\, U\, \sin(45° + \eta/2) \tag{10}$$

where γ'_soil is the unit weight of sand. ΔX and δY are length parameters labelled in Fig. 10. The potential energy gain on the passive side can be calculated similarly. Therefore the

total gravitational energy loss in each stage ΔP can be calculated.

Work done on sand

The work done on the sand can be calculated by integrating separately the shear stress τ with respect to shear strain γ, and the compression stress σ' with respect to volumetric strain ε_v, throughout the volume of the deforming zone. A shear stress–strain relationship for sand was suggested by Oztoprak & Bolton (2013) based on 454 triaxial tests previously published for a variety of sands. The empirical expression for sand secant shear modulus G was linked with shear strain γ by

$$\left(\frac{G}{G_0}\right) = \frac{1}{1 + \left(\frac{\gamma - \gamma_e}{\gamma_r}\right)^a} \tag{11}$$

where G_0 is the elastic modulus at very small strains, γ_r is a reference strain, γ_e is the limiting elastic strain and a is the curvature parameter of the resulting modified hyperbola. Estimates of each of these parameters were given as regressions on basic soil characteristics (e_{max}, e_{min}, U_c), and on the current state of the soil (mean effective stress p' and relative density I_D). For Hostun sand, $U_c = 1{\cdot}637$ can be used, and a curvature parameter $a = 0{\cdot}96$ can be inferred according to Oztoprak & Bolton (2013). For example, regarding the initial condition of loose sand half-way down the wall, at a depth of 80 mm and at 60***g***, $\gamma' = 14{\cdot}2$ kN/m^3 is deduced, so that $\sigma'_v = 68$ kPa, and with $K_0 = 0{\cdot}5$, the mean effective stress $p' = 45$ kPa is obtained. Following the suggested regressions, an elastic stiffness $G_0 = 62330$ kPa, an elastic limit $\gamma_e = 0{\cdot}0006\%$ and a reference strain $\gamma_r = 0{\cdot}03\%$ are obtained.

Some correction is then required to account for the fact that the sand in the centrifuge models begins with an earth pressure coefficient K_0, whereas the sands reported by Oztoprak & Bolton (2013) were tested conventionally from an isotropic stress state. Following the same simplifying procedure used by Vardanega & Bolton (2011), the stress–strain curve (11) was shifted vertically to meet the initial shear stress condition. The maximum shear stress τ in the 1–3 plane can then be expressed by

$$\tau = \tau_0 + G\gamma \tag{12}$$

where τ_0 is the initial shear stress.

The peak mobilised angle of friction of sand in plane strain conditions ϕ'_{max} suggested by Bolton (1986) is used as an upper bound for the shear stress calculation

$$\tau \leqslant s' \sin \phi'_{max} \tag{13}$$

where s' is the mean effective stress on the 1–3 plane.

For a typical slice shown in Fig. 10, the shear stress τ_p on the PQ plane is

$$\tau_p = \tau \cos \eta \tag{14}$$

The normal stress on the plane σ'_p is

$$\sigma'_p = s' + \tau \sin \eta \tag{15}$$

Although the soil in each test was placed at a uniform density, it must be recognised that the mean effective stress p' in each layer varies with the depth of the centroid of that slice, and with the process of excavation. These differences in p' influence each of the parameters G_0, γ_r and γ_e in equation (11) as specified by Oztoprak & Bolton (2013), and also ϕ'_{max} according to Bolton (1986). These variations were accounted for in the analysis.

At each stage, the cumulative strain within each layer can be calculated by adding up incremental shear strains from the previous stages. Work done on the retained side by sand shear in each slice is then calculated, and the total shear work done in each stage of excavation is derived by summing over all slices

$$\Delta W_{sh} = \sum_{layers\_\delta Y}^{Y_m} \left(\int_{\gamma_{stage\_initial}}^{\gamma_{stage\_final}} \tau_p d\gamma \right) \Delta X \delta Y \tag{16}$$

Strain $d\varepsilon_p$ normal to the PQ plane is $d\gamma_p \tan\eta$ according to the assumption of a constant contraction angle. Applying this flow rule to each slice, the total work done by volumetric compression in each stage is found by summing over all slices

$$\Delta W_{vol} = \sum_{layers\_\delta Y}^{Y_{max}} \left(\int_{\gamma_{stage\_initial}}^{\gamma_{stage\_final}} \sigma'_p \, d\varepsilon_p \right) \Delta X \, \delta Y \tag{17}$$

Total soil work on the retained side $\Delta W_{soil,}$ is the sum of these terms

$$\Delta W_{soil,r} = \Delta W_{sh} + \Delta W_{vol} \tag{18}$$

On the excavated side, a similar calculation process is used except that the deformation in Fig. 12 is taken to be pure shear, with no volumetric strain (i.e. no dilation), which therefore entails zero compression energy. The total soil work done during any stage ΔW_{soil} is found as the sum of the work done on the retained side and on the excavated side.

Elastic energy stored in wall flexure

The bending moments in the wall are estimated by assuming Rankine's fully active pressure on the retained side of the wall. The horizontal pressure distribution on the excavated side is also assumed to be linear, with its magnitude calculated according to moment equilibrium at the base. Fig. 13 shows typical measured bending moment profiles for the loose sand excavated to 80 mm and 116 mm, compared in each case with the bending moments calculated following the simplified procedure described above. The overestimation will be due in part to the influence of wall friction reducing active pressures. A larger contribution to the overestimation will be due to the simplifying assumption of a linear distribution of mobilised passive earth pressure beneath the excavation. There is good evidence that mobilised passive earth pressures show a curved distribution, with greater values of the earth pressure coefficient at shallower depths: see Li *et al.* (2014). This effect raises the lever-arm of the passive pressures, reducing calculated bending moments compared with those calculated using linear coefficients and presented as the Rankine estimate in Fig. 13. For convenience of calculation, the Rankine estimate was used in the subsequent assessment of energy flow. It will become obvious that even doubling this will have little effect on the overall energy balance.

Therefore, the total elastic energy in wall flexure can be derived as

$$W_{wall} = \int_{Wall\_length} \frac{1}{2EI} M_w^2 \, dy \tag{19}$$

where M_w is the wall bending moment and EI is the bending stiffness of the wall with a unit width. In each stage, the incremental elastic energy in the wall ΔW_{wall} is then the difference before and after the stage.

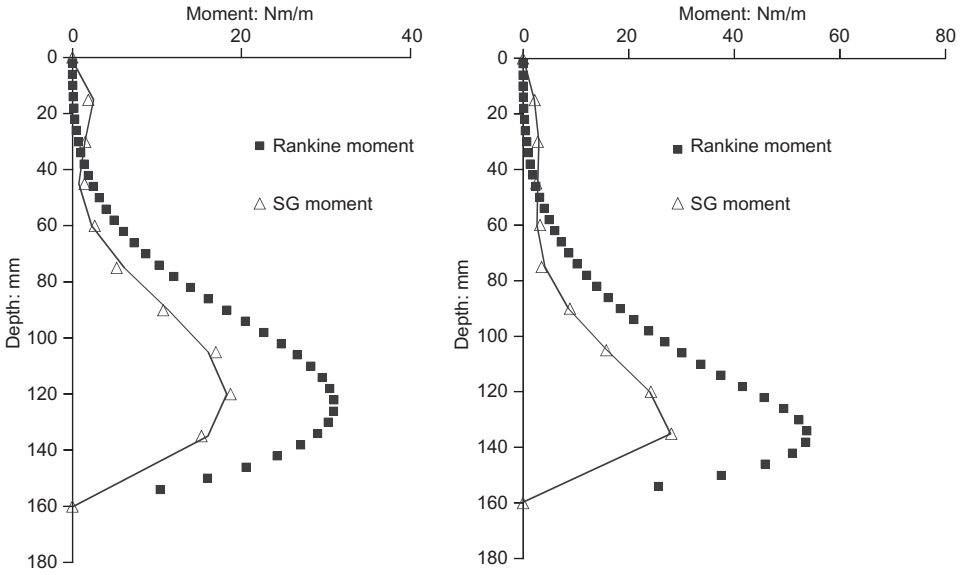

Fig. 13. Comparison between Rankine estimations of bending moment and strain gauge measurements: excavation in loose sand to (a) 80 mm, (b) 116 mm

Friction loss at strongbox boundaries (back wall and window)

Although friction between the sand and the retaining wall is ignored throughout in order to preserve the self-consistency of the deformation mechanism, that between the sand and the strongbox inner surfaces can be accounted for, at least approximately. It is assumed that the intermediate stress acting horizontally on the front and rear faces is not affected by ground movement due to excavation, and that sliding movements can be estimated directly from the plane strain mechanism. In each slice, the average horizontal stress on the boundary is assumed to be the same as the stress at the slice centre. If the depth of the slice centre is y_G, then the friction energy loss on the retained side can be expressed as

$$\Delta W_{\text{bound}} = \sum_{\text{layers\_}\delta Y}^{Y_m} K_0 \gamma'_{\text{soil}} y_G 2\mu \Delta X \delta Y U \tag{20}$$

where horizontal earth pressure ratio $K_0 = 1 - \sin\phi'_{\text{crit}}$ is assumed, as justified by earth pressure measurements in other centrifuge model tests with the same sand (Li *et al.*, 2014). An average friction ratio $\mu = 0{\cdot}27$ between the sand and the strongbox inner surfaces is used, following various direct shear tests (Li, 2013). The calculated result is then adjusted to be equivalent to unit width. The frictional energy loss on the excavated side is calculated similarly.

Energy conservation check of centrifuge test results

If all the procedures for fitting mechanisms and deriving soil responses were correct, the calculated loss of gravitational potential energy should balance the work done in internal sand shearing, wall flexure and friction loss at the boundaries

$$\Delta P = \Delta W_{\text{soil}} + \Delta W_{\text{wall}} + \Delta W_{\text{bound}} \tag{21}$$

The calculations for each energy term were programmed in Matlab 2012b (Mathworks Ltd). Table 2 and Table 3 show energy changes on both sides of the wall in the loose sand test.

Work done at the boundaries is less than 5% of the potential energy loss in each stage, which demonstrates that friction at the strongbox inner surface is not significant in energy transfer. All energy change terms on the passive side are much smaller than on the active side. Therefore, compared to the active side, the movement mechanism on the passive side is of secondary importance, justifying its very simplified treatment. The negative potential energy loss on

Table 2. Energy calculation on the active side of loose sand test

Stage: mm	Potential energy loss ΔP: 10^{-3} J/m	Work done by sand shear, ΔW_{sh}: 10^{-3} J/m	Work done by sand compression, ΔW_{vol}: 10^{-3} J/m	Work done at boundaries, ΔW_{bound}: 10^{-3} J/m
0–60	318·9	118·1	180·9	13·4
60–80	769·2	293·5	433·3	32·3
80–100	2938·2	1121·2	1655·0	123·6
100–116	9914·9	3783·4	5584·9	417·0

Table 3. Energy calculation on the passive side of loose sand test

Stage: mm	Potential energy loss, ΔP_p: 10^{-3} J/m	Work done by sand shear, $\Delta W_{\text{soil,p}}$: 10^{-3} J/m	Work done at boundaries, $\Delta W_{\text{bound,p}}$: 10^{-3} J/m
0–60	−16·5	−1·4	0·5
60–80	−10·9	1·0	0·2
80–100	−5·3	0·8	0·1
100–116	−0·4	0·0	0·0

the passive side indicates that the potential energy increases due to the upward movement. During the 0–60 mm excavation stage, negative work is done on the sand by shearing, due to the initially negative shear stress and positive shear strain. This can be explained by considering a square element of sand on the excavated side. The boundaries of the square element are horizontal and vertical. If the horizontal compression strain in a stage is ε_h, then the vertical extension strain is also ε_h, as the total volume change is assumed to be zero. The total work done of a unit volume in the stage is

$$\Delta W = K\sigma'_v\varepsilon_h + \sigma'_v(-\varepsilon_h) = -(1-K)\sigma'_v\varepsilon_h \quad (22)$$

In the equation, K is the horizontal earth pressure coefficient. At a small excavation depth, K is smaller than 1, so soil work is negative. This is best regarded as elastic recovery. As excavation goes deeper, K increases and soil work become positive.

Energy consumed by sand contraction on the retained side is about 60% of the overall potential energy change. This demonstrates that the tendency for loose sand to 'collapse' during shear is significant.

The different energy terms for the loose sand test are summed in terms of category and shown in Table 4. The errors of global energy conservation are calculated. It is shown that the largest absolute errors are less than 0·02 J/m, which is equivalent to an underestimation of only 2 g of sand moving downwards 3 mm at 60***g*** in the centrifuge package. This magnitude of error is considered negligible in the energy conservation calculation. Relative errors are within 7% for all stages. This lends support to the various simplifying assumptions that were necessary in the analysis.

In the cantilever test in dense sand, energy changes in each stage are also calculated, as shown in Table 5 and Table 6. The energy changes are much smaller than those in loose sand, owing to the much smaller soil movement. Energy change on the excavated side is again negligible compared to energy change on the retained side.

The summary of the energy changes during excavation in the dense sand test is shown in Table 7. Relative errors are within 3% for all stages.

The energy changes for different stages of excavation against the cantilever wall are categorised and quantified in this section. A remarkably good energy balance has been demonstrated at each stage in each test, based on the simplified deformation mechanisms. The main stream of energy flow is from the potential energy to work done on the retained sand. The strain energy in the retaining wall, calculated using linear pressure distributions based on Rankine active values, was always less than 3% of the total energy flow, and usually much less. Although the measured strain energy was up to double the calculated value, this is still negligible.

Table 4. Energy conservation error in loose sand test

Stage: mm	Total potential energy loss: 10^{-3} J/m	Total work done in sand: 10^{-3} J/m	Elastic energy at wall ΔW_{vol}: 10^{-3} J/m	Total work done at boundaries: 10^{-3} J/m	Absolute error: 10^{-3} J/m	Relative error: %
0–60	302·4	297·6	11·4	13·9	−20·5	−6·8
60–80	758·4	727·8	10·2	32·6	−12·2	−1·6
80–100	2932·9	2777·0	14·4	123·6	17·9	0·6
100–116	9914·5	9368·3	15·0	417·0	114·2	1·2

Table 5. Energy calculation on the retained side of dense sand test

Stage: mm	Potential energy loss ΔP: 10^{-3} J/m	Work done by sand shear ΔW_{sh}: 10^{-3} J/m	Work done by sand compression ΔW_{vol}: 10^{-3} J/m	Work done at boundaries ΔW_{bound}: 10^{-3} J/m
0–105	191·7	158·7	14·8	9·6
105–111	94·1	80·5	7·1	4·7
111–117	161·5	138·1	12·1	8·1

Table 6. Energy calculation on the excavated side of dense sand test

Stage: mm	Potential energy loss, ΔP_p: 10^{-3} J/m	Work done by sand shear, $\Delta W_{soil,p}$: 10^{-3} J/m	Work done at boundaries, $\Delta W_{bound,p}$: 10^{-3} J/m
0–105	−0·3	0·0	0·0
105–111	0·0	0·0	0·0
111–117	0·0	0·0	0·0

Table 7. Energy conservation error in dense sand test

Stage: mm	Total potential energy loss: 10^{-3} J/m	Total work done in sand: 10^{-3} J/m	Elastic energy in wall, ΔW_{vol}: 10^{-3} J/m	Total work done at boundaries: 10^{-3} J/m	Absolute error	Relative error: %
0–105	191·4	173·5	3·0	9·6	5·3	2·8
105–111	94·1	87·6	2·7	4·7	−1·0	−1·0
111–117	161·5	150·2	3·8	8·1	−0·7	−0·4

DISCUSSION

A key objective of retaining wall design is to restrict the soil movement behind the wall in order to protect adjacent buildings and services from damage. In the analysis of Boscardin & Cording (1989) the damage to such buildings is related to the maximum angular distortion β_{max} and horizontal strain ε_h induced in the foundations by deformations within the retained ground. If the building is also considered to be relatively light and flexible, the deformation of the foundations will be equal to the corresponding deformations of the soil beneath, and equivalent to that of a greenfield site. Boscardin & Cording (1989) suggest that this will be the case for buildings of up to three storeys, but if the relative stiffness of the building is more significant a reduction factor will apply, as recommended by Goh & Mair (2012). In what follows it will be assumed that the facility of interest is flexible, such as a low-rise masonry building on individual strip footings running parallel to the retaining wall. The newly described deformation mechanism can then be used to assess the influence of cantilever wall excavation in sands.

According to the simplified deformation mechanism, the settlement v on the surface of retained sand can be derived as

$$v = 1{\cdot}3U_{Xm}\frac{\sin\Omega}{\cos\eta}\left(1-\frac{x}{H}\cot\Omega\right)\left(0{\cdot}77-\frac{x}{h}\cot\Omega\right) \quad (23)$$

for $x \leqslant 0{\cdot}77H{\cdot}\tan\Omega$, where $\Omega = 45°+\eta/2$, and x is the horizontal distance from the excavation.

Therefore if the flexural stiffness of the interacting structure is ignored, the maximum angular distortion β_{max} of a long brick wall perpendicular to the retaining wall should be

$$\beta_{max} = 2{\cdot}3\frac{U_{Xm}}{H}\frac{\cos\Omega}{\cos\eta} \quad (24)$$

Similarly the horizontal soil movement on the soil surface u is

$$u = 1{\cdot}3U_{Xm}\frac{\cos\Omega}{\cos\eta}\left(1-\frac{x}{H}\cot\Omega\right)\left(0{\cdot}77-\frac{x}{H}\cot\Omega\right) \quad (25)$$

And the maximum horizontal shear strain ε_{hm} is

$$\varepsilon_{hm} = 2{\cdot}3\frac{U_{Xm}}{H}\frac{\cos^2\Omega}{\sin\Omega\ \cos\eta} \quad (26)$$

According to equation (24) and equation (26), the damage trajectory of a cantilever wall excavation can be plotted after Boscardin & Cording (1989) as shown in Fig. 14 for the negative angles of dilatancy that are consistent with small magnitudes of soil strain. Cantilever wall excavations in dense sand ($I_D \sim 0{\cdot}85$) with an angle of dilatancy $-4°$, and loose sand ($I_D \sim 0{\cdot}45$) with an angle of dilatancy $-32°$, are each indicated in the figure, falling inside the zone proposed by Boscardin & Cording (1989) as applicable to shallow mines, braced cuts and tunnels. The extent of those distortions at a given stage in each of the two centrifuge tests, representing the behaviour of a heavy-duty sheet pile wall, is also marked in Fig. 14. For the loose sand test, the proportion of excavation is chosen to be $h/H = 0{\cdot}5$, and for the dense sand test $h/H = 0{\cdot}66$. Further work is underway to generalise these results.

CONCLUSIONS

Two centrifuge models were tested to investigate cantilever wall excavations in sands with different relative densities. In-flight excavation was performed, and soil movements during the excavation were observed. A simple deformation mechanism was proposed according to the experimental observations. The energy flow in the deformation mechanism was back-analysed in the two centrifuge tests, and energy conservation was confirmed within 7% error.

In these two examples, the lost potential energy is mainly consumed in sand shear and compression. The elastic energy in the wall and the energy lost in friction at the soil strongbox boundary are relatively small. Also, the energy transfer mainly happens on the active side and energy changes on the passive side are small in comparison. This style of energy audit should be beneficial in other applications to check the consistency of assumed deformation mechanisms fitted to soil boundary measurements and analysed using soil stress–strain relations derived from element tests. Were such audits to show an imbalance of energy, this would indicate either that the internal soil deformation mechanisms were not as assumed or, more likely, that the soil element test data were inadequate for the back-analysis.

Validated deformation mechanisms can be useful in practice. The inferred soil movement mechanism can be used to evaluate the damage to adjacent low-rise buildings according to Boscardin & Cording (1989). It was shown that the lateral extent of the zone of deformation, and the relationship between angular distortion and horizontal strain beside a cantilever wall excavation, depend on the (negative) angle of dilatancy mobilised in the sand at a corresponding strain, and therefore on its relative density.

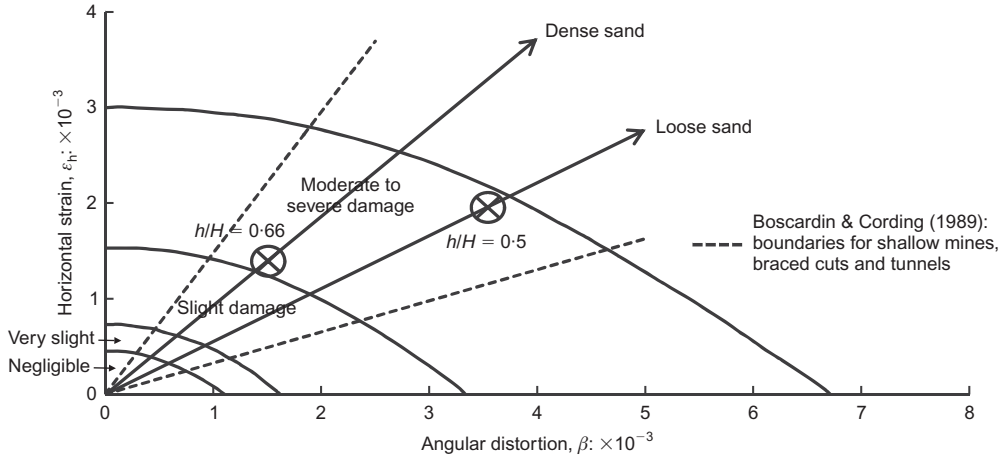

Fig. 14. Influence of excavation in sands to adjacent buildings (plotted after Boscardin & Cording, 1989)

ACKNOWLEDGEMENT

Dr Li was supported by Cambridge Overseas Trust and the China Scholarship Council.

NOTATION

a curvature parameter
c curve fitting parameter
D_{10} diameter of soil particles for which 10% of the particles are finer
D_{30} diameter of soil particles for which 30% of the particles are finer
D_{50} mean grain size
D_{60} diameter of soil particles for which 60% of the particles are finer
d wall embedment depth
$d\varepsilon_p$ incremental normal strain on the thin slice
EI bending stiffness of the wall
G secant shear modulus
G_0 elastic shear modulus
H total wall height
h excavation depth
I_D relative density
K horizontal earth pressure ratio
K_0 lateral earth pressure ratio at rest
M_w wall bending moment
s' mean effective stress on the 1–3 plane
U total soil movement in X-Y coordinate system
U_c uniformity coefficient
U_X soil movement component parallel to axis X
U_{Xm} maximum U_X in the deformation mechanism on the active side
u horizontal displacement
v vertical displacement (settlement)
W_{wall} total elastic energy stored in wall
X coordinate of the axis which is parallel to mechanism boundary line
x horizontal coordinate, distance from the excavation
Y coordinate of the axis which is vertical to mechanism boundary line
Y_{max} maximum coordinate on Y axis in the triangle mechanism
y vertical coordinate, depth on the retained side
α average soil surface inclination angle
β average wall inclination angle
β_{max} the maximum angular distortion on the retained side
γ shear strain, the diameter of the Mohr strain circle
γ_e elastic threshold strain
γ_r reference shear strain
γ'_{soil} sand unit weight
ΔP total gravitational energy loss in a stage
ΔP_r total gravitational energy loss on the retained side in a stage
ΔW_{bound} energy loss due to friction at side of the strongbox during a stage
ΔW_{sh} work done by sand shear in a stage
ΔW_{soil} total work done in sand in a stage
$\Delta W_{soil,r}$ total work done in sand on the retained side in a stage
ΔW_{wall} change of elastic energy stored in wall during a stage
ΔW_{vol} work done by sand contraction in a stage
ΔX width of the sand layer (Active side)
δY slice thickness
$\delta\gamma$ incremental shear strain
$\delta\varepsilon_h$ incremental horizontal soil strain
$\delta\varepsilon_v$ incremental vertical soil strain
$\delta\varepsilon_{vol}$ incremental volumetric strain
$\delta\varepsilon_s$ incremental engineering shear strain
ε_h horizontal strain on the soil surface
ε_{hm} maximum horizontal strain on the soil surface
ε_{vol} volumetric strain
ε_1 major principle strain
ε_3 minor principle strain
η contraction angle (negative of dilation angle)
θ inclination angle of deformation boundary line angle
μ average friction ratio between sand and strongbox inner face
ν dilation angle
σ'_h horizontal earth pressure
σ'_p effective normal stress on a thin slice
σ'_v vertical earth pressure
τ shear stress, the radius of the Mohr stress circle
τ_p shear stress on a thin slice
ϕ'_{crit} critical state angle
ϕ'_{max} peak shear angle
Ω $45°+\eta/2$

REFERENCES

Bolton, M. D. (1986). The strength and dilatancy of sands. *Géotechnique* **36**, No. 1, 65–78, http://dx.doi.org/10.1680/geot.1986.36.1.65.

Boscardin, M. D. & Cording, E. J. (1989). Building response to excavation-induced settlement. *J. Geotech. Engng* **115**, No. 1, 1–21.

Bransby, P. L. & Milligan, G. W. E. (1975). Soil deformations near cantilever sheet pile walls. *Géotechnique* **25**, No. 2, 175–195, http://dx.doi.org/10.1680/geot.1975.25.2.175.

Clough, G. W. & O'Rourke, T. D. (1990). Construction induced movements of insitu walls. *Proceedings of ASCE special conference, Design and performance of earth retaining structures*, Cornell University, Ithaca, New York, USA, (eds P. Lambe and L. A. Hansen), Geotechnical Special Publication no. 25, pp. 439–470. New York, NY, USA: ASCE.

Goh, K. H. & Mair, R. J. (2012). The response of buildings to movements induced by deep excavations. *Proceedings of the 7th international symposium on geotechnical aspects of underground construction in soft ground*, Rome, Italy (ed. G. Viggiani), pp. 903–910. Boca Raton, Florida, USA: CRC Press.

Haigh, S. K., Houghton, N. E., Lam, S. Y., Li, Z. & Wallbridge, P. J. (2010). Development of a 2D servo-actuator for novel centrifuge modelling. *Proceedings of the 7th international conference of physical modelling in geotechnics*, Zurich, Switzerland (eds S. Springman, J. Laue and L. Seward), pp. 239–244. Boca Raton, Florida, USA: CRC Press.

Lam, S. Y. & Bolton, M. D. (2011). Energy conservation as a principle underlying mobilizable strength design for deep excavations. *J. Geotech. Geoenviron. Engng* **137**, No. 11, 1062–1074.

Li, Y. (2013). *Ground movements due to excavation in cohesionless soil: physical and analytical models*. PhD thesis, University of Cambridge, Cambridge, UK.

Li, Y., Talesnick, M. L. & Bolton, M. D. (2014). Use of null gauges to monitor soil stresses during excavation in a centrifuge. *Int. J. Phys. Modelling Geotech*. **14**, No. 2, 40–53.

Madabhushi, S. P. G., Houghton, N. E. & Haigh, S. K. (2006). A new automatic sand pourer for model preparation at University of Cambridge. *Proceedings of the 6th international conference of physical modelling in geotechnics*, Hong Kong (eds C. W. W. Ng, Y. H. Wang and L. M. Zhang), pp. 217–222. Leiden, the Netherlands: CRC Press/Balkema.

Osman, A. S. & Bolton, M. D. (2004). A new design method for retaining walls in clay. *Can. Geotech. J.* **41**, No. 3, 451–466.

Oztoprak, S. & Bolton, M. D. (2013). Stiffness of sands through a laboratory test database. *Géotechnique* **63**, No. 1, 54–70, http://dx.doi.org/10.1680/geot.10.P.078.

Peck, R. B. (1969). Deep excavations and tunneling in soft ground. *Proceedings of the 7th international conference on soil mechanics and foundation engineering, State-of-the-art volume*, Mexico City, Mexico, pp. 225–290. Mexico City, Mexico: Sociedad Mexicana de Mecánica de Suelos.

Powrie, W. (1986). *The behaviour of diaphram walls in clay*. PhD thesis, University of Cambridge, Cambridge, UK.

Stringer, M. E. (2012). *The axial behaviour of piled foundations in liquefiable soil*. PhD thesis, University of Cambridge, Cambridge, UK.

Vardanega, P. J. & Bolton, M. D. (2011). Strength mobilization in clays and silts. *Can. Geotech. J.* **48**, No. 10, 1485–1503.

White, D. J., Take, W. A. & Bolton, M. D. (2003). Soil deformation measurement using particle image velocimetry (PIV) and photogrammetry. *Géotechnique* **53**, No. 7, 619–631, http://dx.doi.org/10.1680/geot.2003.53.7.619.